

## Mg-Air Batteries

How to cite: *Angew. Chem. Int. Ed.* **2021**, *60*, 15317–15322

International Edition: doi.org/10.1002/anie.202104536

German Edition: doi.org/10.1002/ange.202104536

# High-Energy-Density Magnesium-Air Battery Based on Dual-Layer Gel Electrolyte

Luhe Li, Hao Chen, Er He, Lie Wang, Tingting Ye, Jiang Lu, Yiding Jiao, Jiacheng Wang, Rui Gao, Huisheng Peng,\* and Ye Zhang\*

**Abstract:** Mg-air batteries are explored as the next-generation power systems for wearable and implantable electronics as they could work stably in neutral electrolytes and are also biocompatible. However, high corrosion rate and low utilization of Mg anode largely impair the performance of Mg-air battery with low discharge voltage, poor specific capacity and low energy density. Here, to the best of our knowledge, we first report a dual-layer gel electrolyte to simultaneously solve the above two problems by preventing the corrosion of Mg anode and the production of dense passive layer, respectively. The resulting Mg-air batteries produced an average specific capacity of 2190 mAhg<sup>-1</sup> based on the total Mg anode (99.3% utilization rate of Mg anode) and energy density of 2282 Whkg<sup>-1</sup> based on the total anode and air electrode, both of which are the highest among the reported Mg-air batteries. Besides, our Mg-air batteries could be made into a fiber shape, and they were flexible to work stably under various deformations such as bending and twisting.

Wearable and implantable electronic devices represent the next-generation electronics and are booming rapidly in the recent decade.<sup>[1–3]</sup> To stably and long-termly power these electronic devices, it is critical to make matchable and safe energy storage devices.<sup>[4–7]</sup> To this end, metal-air batteries with high energy densities have attracted increasing interests.<sup>[8,9]</sup> Among them, Mg-air batteries work stably in neutral electrolytes and are also biocompatible as Mg<sup>2+</sup> ions are harmless to the human body.<sup>[10–12]</sup> Therefore, Mg-air batteries are explored as promising candidates on the skin and inside the body.

However, the high corrosion rate and low utilization of Mg anode largely impair the performance of Mg-air batteries (Figure 1a).<sup>[13,14]</sup> After the active Mg anode contacted the aqueous electrolyte, the following side reaction occurs: Mg + H<sub>2</sub>O → Mg(OH)<sub>2</sub> + H<sub>2</sub>.<sup>[15]</sup> The electrons are directly transferred to the H<sup>+</sup> in the electrolyte without passing through the external circuit, leading to a colossal capacity loss. Besides, a dense and insoluble passive layer formed on the surface of Mg anode during both discharge and corrosion processes prevents Mg anode and electrolyte from contacting each other, resulting in low Mg utilization.<sup>[16]</sup> As a result, the current Mg-air batteries typically show low discharge voltage, poor specific capacity and low energy density.

Mg alloying and corrosion-inhibiting electrolytes have been most investigated to improve the electrochemical properties of Mg-air batteries.<sup>[16–20]</sup> The incorporation of Al and Zn into Mg improved its corrosion resistance to a certain extent, but it led to a lower discharge voltage because of the passive layer attached to the surface of Mg anode.<sup>[16,17,21]</sup> Although adding the other metals of Pb, Hg and Ga into Mg improved the discharge voltage, they were harmful to human health and the environment.<sup>[22,23]</sup> Besides, the added metal elements cannot be discharged in the neutral electrolyte, which reduced the capacity of Mg-air batteries. Corrosion-inhibiting electrolytes decreased the Mg corrosion by forming a protective layer on the surface of Mg anode, but the discharge produced passive layer that was still firmly attached to the Mg anode, inhibiting the full utilization of Mg anode.<sup>[19]</sup>

Herein, we have first presented a dual-layer gel electrolyte to simultaneously solve these problems of Mg-air batteries (Figure 1b). The dual-layer gel electrolyte prevented the corrosion of Mg anode and the production of dense passive layer, which avoided the consumption of Mg anode due to the side reaction and increased the utilization of Mg in the discharge process, thus improving the capacity and energy density of the battery. As a result, our Mg-air batteries produced an average specific capacity of 2190 mAhg<sup>-1</sup> based on the total weight of Mg anode and an energy density of 2282 Whkg<sup>-1</sup> based on the weight of anode and air electrode, which both far exceed the available Mg-air batteries. Besides, the Mg-air battery had been made into a fiber shape with high flexibility, and it could accommodate various deformations with stable power output.

Pure Mg was polished and used as the anode (Figure S1), and the dual-layer gel electrolyte consisting of organic gel and hydrogel was evenly coated on the surface of Mg anode subsequently. MnO<sub>2</sub>/carbon nanotube (CNT) sheets were wrapped outside to work as air electrode. Aligned CNT sheets were chosen as current collectors due to their lightweight,

[\*] L. Li, H. Chen, E. He, Dr. L. Wang, T. Ye, J. Lu, Y. Jiao, J. Wang, R. Gao, Prof. Y. Zhang  
 National Laboratory of Solid State Microstructures, Jiangsu Key Laboratory of Artificial Functional Materials, Chemistry and Biomedicine Innovation Center (ChemBIC), Collaborative Innovation Center of Advanced Microstructures,  
 College of Engineering and Applied Sciences, Nanjing University  
 Nanjing 210023 (China)  
 E-mail: yezhang@nju.edu.cn

Prof. H. Peng  
 State Key Laboratory of Molecular Engineering of Polymers, Department of Macromolecular Science and Laboratory of Advanced Materials, Fudan University  
 Shanghai 200438 (China)  
 E-mail: penghs@fudan.edu.cn

 Supporting information and the ORCID identification number(s) for the author(s) of this article can be found under:  
 <https://doi.org/10.1002/anie.202104536>

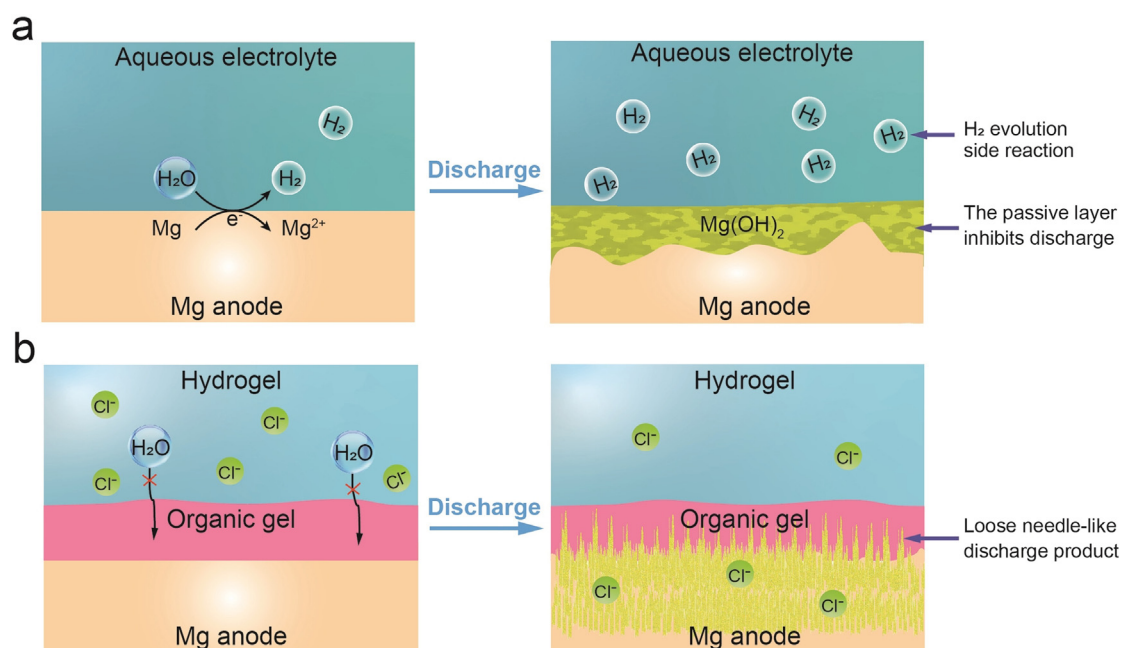


**Figure 1.** Discharge process of the Mg-air batteries in the different electrolytes. a) In conventional aqueous electrolytes, the  $\text{H}_2$  evolution side reaction occurs at the anode-electrolyte interface. The side reaction and discharge process both produce a dense  $\text{Mg}(\text{OH})_2$  passive layer, which separates the anode and electrolyte, leading to battery failure. b) The proposed dual-layer gel electrolyte efficiently protects the Mg anode from corrosion and endows a loose needle-like discharge product, which keeps the discharge process active until the Mg anode was fully consumed.

porous, conductive, and flexible features (Figure S2).<sup>[24]</sup> The  $\text{MnO}_2$  nanowires were uniformly dispersed on the CNT sheets (Figure S3), and the formed nano-sized voids among the hybrid  $\text{MnO}_2/\text{CNT}$  sheets favored a highly efficient diffusion of air.

The dual-layer gel electrolyte was composed of poly(ethylene oxide) (PEO) organic gel and crosslinked polyacrylamide (PAM) hydrogel (Figure 2a). The PEO organic gel and PAM hydrogel were selected because of their high ionic conductivity and formation of good interface. The PEO gel exhibited a smooth, uniform and dense surface (Figure 2b). Besides, due to the low crystallinity of the organic gel, the high ionic conductivity of  $4.32 \text{ mS cm}^{-1}$  was obtained (Figure S4). The PAM hydrogel exhibited a porous network structure with ionic conductivity of  $52.61 \text{ mS cm}^{-1}$  (Figure 2c and Figure S5). This dual-layer gel electrolyte showed a stable interface. As revealed by confocal laser scanning microscopy (Figure 2d) and scanning electron microscopy (SEM) in Figure S6, the two gel electrolytes closely contacted each other without obvious gaps at the interface. Besides, the dual-layer gel electrolyte exhibited shear stress of 2.8 kPa, manifesting the strong adhesion between PAM and PEO gel. Moreover, after bending the dual-layer gel electrolyte at  $90^\circ$  for 5000 cycles, we found the shear stress slightly increased to 4.5 kPa, and the ionic conductivities remained almost unchanged (Figure 2e and f). Therefore, the dual-layer gel electrolyte owned a stable interface, which was essential for flexible batteries. The high compatibility between the two gels and impressive interface stability might result from the hydrogen bonds formed through the functional groups in PAM and PEO.<sup>[25,26]</sup> As a result, benefitted from the high ionic conductivity of the organic gel and the hydrogel and their

stable interface, the dual-layer gel electrolyte delivered a relatively high ionic conductivity of  $6.52 \text{ mS cm}^{-1}$  (Figure S7).

More importantly, the organic PEO gel can efficiently prevent the corrosion of Mg metal. Here, another two kinds of commonly used polymer gels, i.e., poly(vinylidene fluoride-co-hexafluoropropylene) (PVDF) and thermoplastic polyurethane (TPU), were also studied as a comparison. As shown in Figure 2g, after placed in PAM hydrogel for 6 h, the Mg foil without organic gel suffered serious corruptions. The Mg foil lost its bright metallic luster and turned gray, producing a large number of bubbles. In contrast, the Mg foils protected with the organic gel underwent minor corruptions. A small number of bubbles can still be observed for the PVDF and TPU, and the PEO-protected Mg foil remained unchanged and no bubbles appeared, proving the effective protection of Mg anode. On the other hand, the produced hydrogen concentration was monitored by gas chromatography. Consistent with the photograph in Figure 2g, the Mg foil without protective organic gel emitted the highest hydrogen concentration, and the PEO-protected Mg foil showed the lowest hydrogen emission among the three organic gels (Figure 2h). The protection of organic gels was also verified in the LiCl aqueous electrolyte. After being immersed for 6 h, the PEO-coated Mg foil remained almost unchanged, while visible  $\text{Mg}(\text{OH})_2$  peaks in the X-ray diffraction (XRD) pattern appeared for bare Mg foil and PVDF and TPU-protected Mg foils (Figure 2i). These results indicated that the organic PEO gel most effectively protected the Mg anode from corrosion. In fact, the corrosion rate of the Mg protected with PEO gel was weighted to be  $0.007 \text{ mg cm}^{-2} \text{ h}^{-1}$ , which is seventy-six times lower than that of Mg without protection (Figure S8).

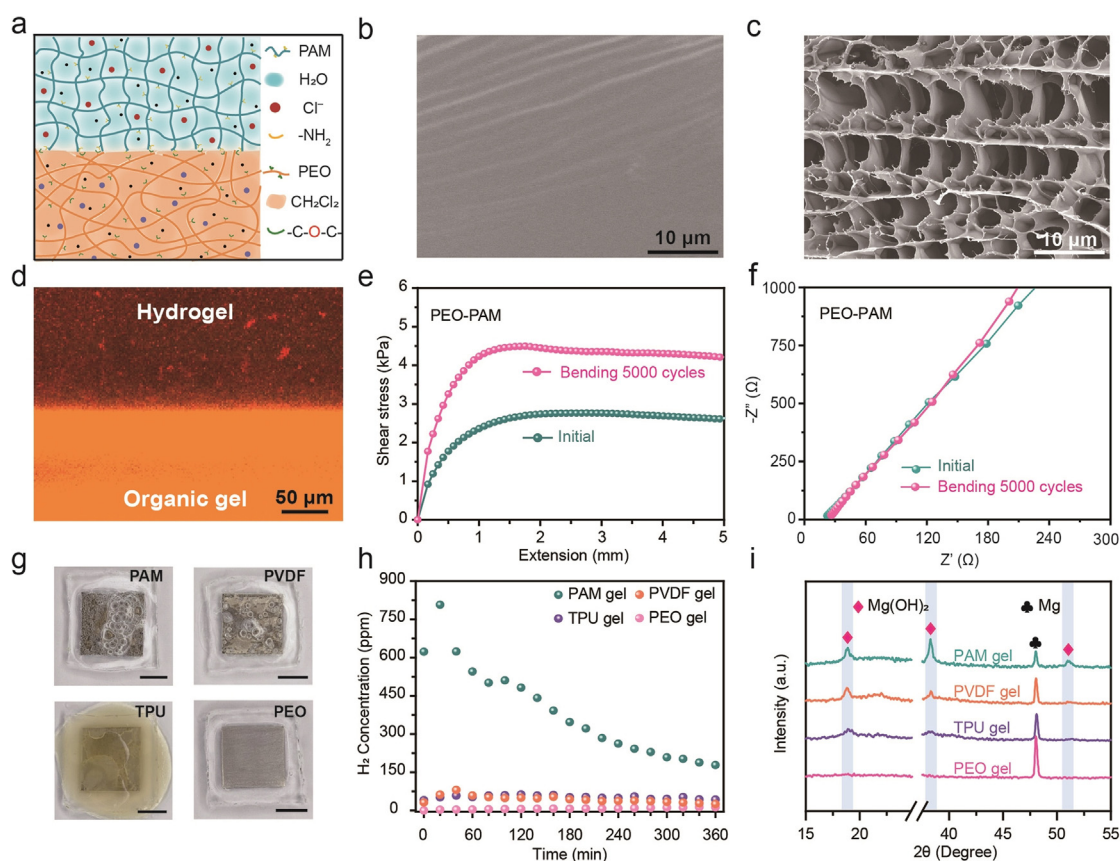


**Figure 2.** Characterization of the dual-layer gel electrolyte. a) Composition of the dual-layer gel electrolyte. b, c) SEM images of organic gel and hydrogel. d) Confocal laser scanning microscopy image showing the well-bonded interface of the dual-layer gel electrolyte. e, f) Shear stress curves and electrochemical impedance spectrum of the dual-layer gel electrolyte before and after bending at  $90^\circ$  for 5000 cycles, respectively. g, h) Photographs and hydrogen concentration of the Mg anodes protected by different organic gels after attached with the PAM hydrogel for 6 h. Scale bar: 5 mm. i) XRD patterns of the PAM hydrogel-coated Mg anode for 6 h and organic gel-protected Mg anode after being immersed in LiCl solution for 6 h.

Compared with the PVDF and TPU gel, the sticky PEO gel can firmly bond with Mg anode to avoid detachment of the protective layer, thus providing more durable protection. Besides, the PEO gel electrolyte showed a smooth, uniform and dense surface, which prolonged the permeation pathway of water molecules and reduced the diffusion rate to enhance protective effects.

Figure 3a shows the representative discharge curves of Mg-air batteries using dual-layer gel electrolyte and PAM hydrogel electrolyte. The Mg-air battery with the dual-layer gel electrolyte was discharged stably for more than 220 h with a working voltage above 1 V. In contrast, the Mg-air battery with a single hydrogel electrolyte was discharged by less than 50 h. To investigate the side reaction during discharging,  $H_2$  concentration was also monitored (Figure 3b). The Mg-air battery using dual-layer gel electrolyte kept  $H_2$  concentration as low as  $\approx 10$  ppm during the whole monitoring period, indicating that the side reaction could be almost ignored. For the Mg-air battery with hydrogel electrolyte, a significantly high  $H_2$  concentration of  $\approx 2000$  ppm at the beginning of discharge was recorded, proving the serious side reaction during discharging. The above results further verified that the

dual-layer gel electrolyte can efficiently protect Mg anode from corrosion and thus improve the anode utilization.

The Mg-air batteries with dual-layer gel electrolyte showed ultrahigh specific capacities of  $2190 \pm 54 \text{ mAh g}^{-1}$  based on the total weight of Mg anode, which almost reached the theoretical value of Mg anode (Figure 3c). The utilization rate of Mg anode reached 99.3%. In contrast, Mg-air batteries with hydrogel electrolyte only showed specific capacities of  $329 \pm 67 \text{ mAh g}^{-1}$ . Attributed to the ultrahigh specific capacity, high discharge voltage and lightweight air electrode, the Mg-air battery with dual-layer gel electrolyte performed a high energy density of  $2282 \text{ Wh kg}^{-1}$  and a power density up to  $550 \text{ W kg}^{-1}$  based on the total weight of anode and air electrode. The Mg-air battery with PAM hydrogel electrolyte only exhibited an energy density of  $399 \text{ Wh kg}^{-1}$  due to the severe corrosion. Compared with the other reported Mg-air batteries, our Mg-air battery using dual-layer gel electrolyte showed the highest specific capacity with a much higher open-circuit voltage (Figure 3d with details shown at Table S1).<sup>[11,15–21,27]</sup> Furthermore, our Mg-air batteries also showed both much higher specific capacity and energy density than the other reported batteries, e.g., the specific capacity is fifteen times higher than a Zn-ion battery and the energy

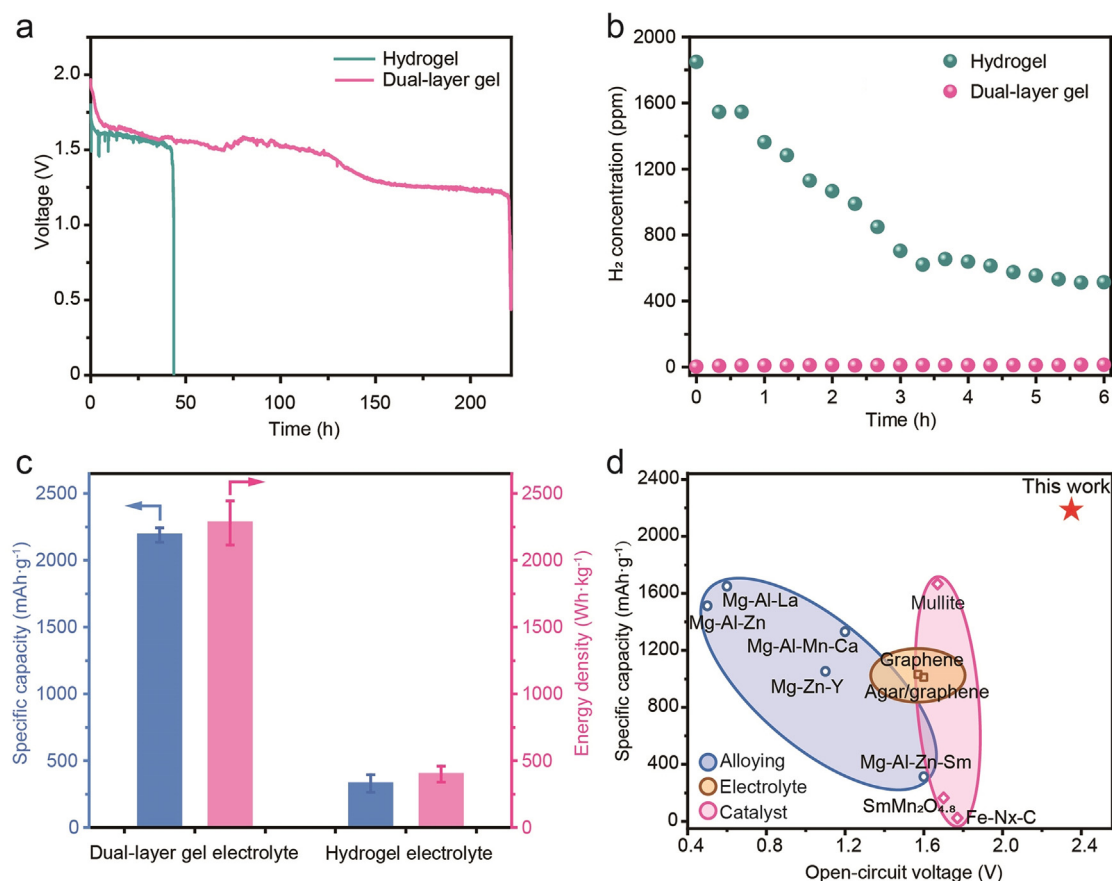


**Figure 3.** Electrochemical performance of the Mg-air battery. a) Representative discharge curves of the Mg-air battery applying dual-layer gel electrolyte and hydrogel electrolyte. b) H<sub>2</sub> concentration of the Mg-air battery after discharged for 6 h using dual-layer gel electrolyte and hydrogel electrolyte. c) Specific capacity and energy density of the Mg-air battery using dual-layer gel electrolyte and hydrogel electrolyte. d) Specific capacity and open-circuit voltage of the Mg-air battery with dual-layer gel electrolyte compared with the previously reported strategies. Alloying: Mg-Al-Zn,<sup>[17]</sup> Mg-Al-Zn-Sm,<sup>[17]</sup> Mg-Al-La,<sup>[18]</sup> Mg-Al-Mn-Ca,<sup>[16]</sup> and Mg-Zn-Y;<sup>[21]</sup> optimized electrolyte: graphene<sup>[19]</sup> and agar/graphene gel;<sup>[20]</sup> catalyst: Fe-Nx-C,<sup>[12]</sup> mullite<sup>[15]</sup> and SmMn<sub>2</sub>O<sub>4.8</sub>.<sup>[27]</sup>

density is about forty-six times of the aqueous lithium-ion battery (Figure S9).<sup>[28–33]</sup>

Besides the high electrochemical performance, the Mg-air battery could be made into a fiber shape with a coaxial structure, and it was flexible (Figure S10). The fiber Mg-air battery performed a stable output voltage after bending to 45°, 90° and 135°. A red light-emitting diode (LED) can be further lighted up and the lighting intensity had been well maintained even when the fiber Mg-air battery was bent to various angles. The fiber Mg-air battery was also bent into a circle to power a clock, and the voltage remained almost unchanged, proving the high flexibility of the fiber Mg-air battery (Figure S11). Moreover, the fiber Mg-air battery kept working for more than 15 h even after being immersed in water (Figure S12). The lighting intensity of the LED kept almost unchanged before and after being immersed in water, suggesting high stability of the Mg-air battery. Interestingly, the Mg-air batteries can use the oxygen dissolved in water to work, so it is promising for them to be used in implantable bioelectronics.

The discharge products of the Mg-air battery were investigated by a combination of SEM and XRD. After discharging for 48 h, the needle-like products were loosely

and vertically grown on the surface of the Mg anode (Figure 4a). Lots of voids among the needle-like discharge products were formed, and the electrolyte can effectively infiltrate into the Mg anode at the bottom. The energy-dispersive X-ray spectroscopy (EDS) elemental mapping suggests that the discharge product mainly consisted of Mg, O, and Cl elements. After being fully discharged, the discharge product was characterized by XRD (Figure S13). The result indicates that the discharge product was Mg<sub>2</sub>Cl(OH)<sub>3</sub>, which differed from the commonly reported Mg(OH)<sub>2</sub> (Figure 4b). The discharge product was further characterized by X-ray photoelectron spectroscopy (XPS). The peak of Cl 2p<sub>3/2</sub> located at 197.1 eV and single Mg 2p peak located at 48.9 eV were confirmed as Cl<sup>-</sup> and Mg<sup>2+</sup>, respectively (Figure 4c and d).<sup>[34,35]</sup> The valency of Cl and Mg ions was consistent with the results of XRD. For the O 1s, it was distinguished into three peaks, which are referred to the adsorbed oxygen species (530.1 eV), OH<sup>-</sup> (531.5 eV) and crystal water (533.23 eV) (Figure 4e).<sup>[36]</sup> Therefore, the overall discharge reaction is: 8Mg + 3O<sub>2</sub> + 6H<sub>2</sub>O + 4Cl<sup>-</sup> → 4Mg<sub>2</sub>Cl(OH)<sub>3</sub> + 4e<sup>-</sup>. In the discharge process, oxygen was reduced at the air electrode and the Mg anode was oxidized to Mg<sup>2+</sup>. Meanwhile, as the PAM hydrogel and PEO gel were

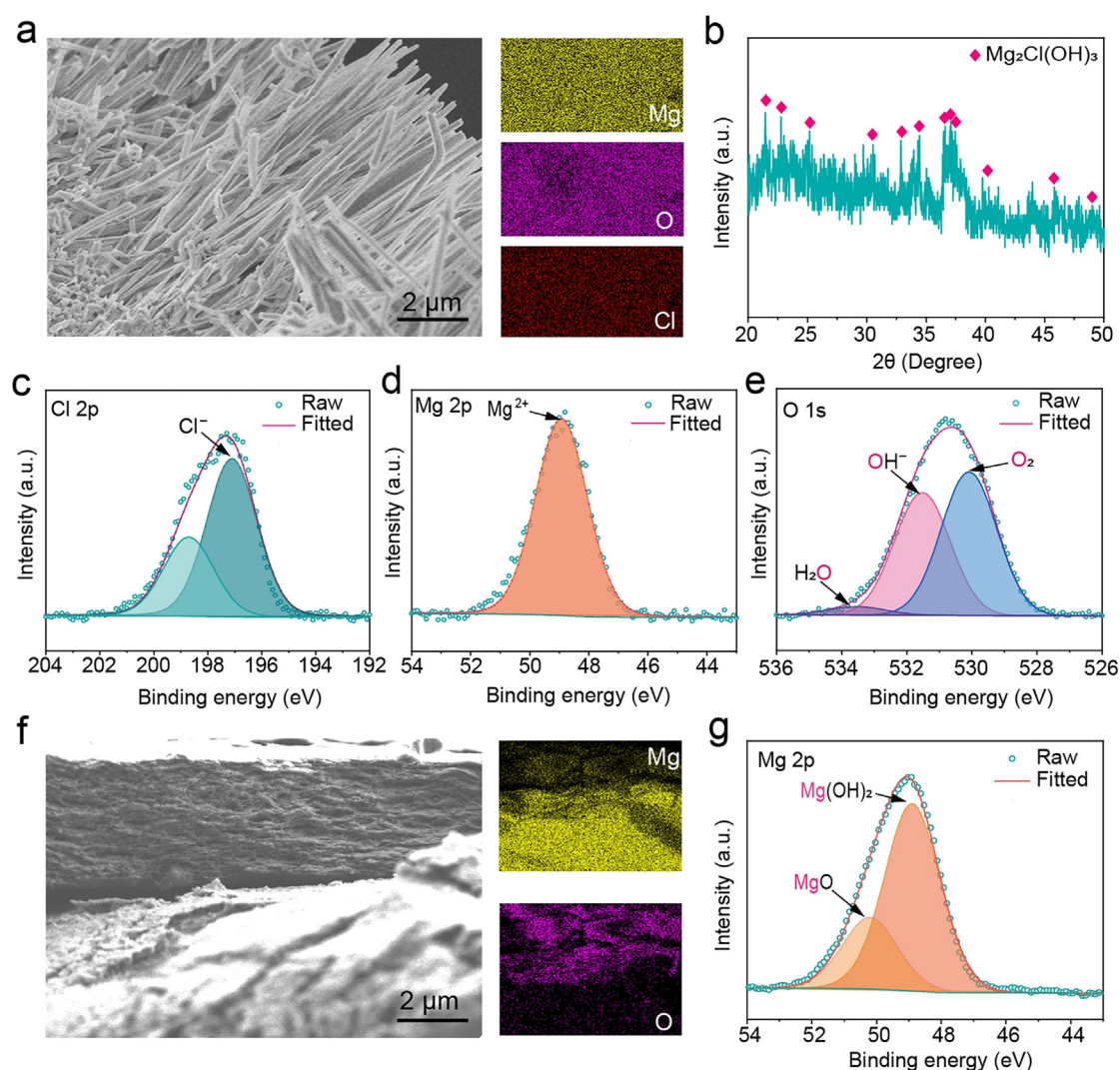


**Figure 4.** Characterization of the discharge products. a) SEM image (left) and EDS elemental mappings (right) of the discharge product using dual-layer gel electrolyte with LiCl in the hydrogel electrolyte. b) Corresponding XRD pattern of the discharge product (ICDD 00-007-0412). c–e) Corresponding XPS spectra of Cl 2p, Mg 2p and O 1s. f) SEM image (left) and EDS elemental mappings (right) of the discharge product using dual-layer gel electrolyte with LiTFSi in the hydrogel electrolyte. g) Corresponding XPS spectrum of Mg 2p of the discharge product.

$\text{Cl}^-$  ions conductive,<sup>[37]</sup> the  $\text{Cl}^-$  ions were migrated through the dual-layer gel electrolyte to the anode driven by potential difference. The formed whiskers of  $\text{Mg}_2\text{Cl}(\text{OH})_3$  were extended in a certain orientation during its crystal growth,<sup>[38]</sup> enabling the specific needle-like morphology.

To verify the reason for forming this unique morphology of the discharge product, the LiCl in the PAM hydrogel was replaced with NaCl, and the discharge products also showed the needle-like morphology (Figure S14). Subsequently, the LiCl in the dual-layer gel electrolyte was replaced by lithium bis(trifluoromethanesulfonyl)imide (LiTFSi) to fabricate the Mg-air battery. The resulting Mg-air battery only showed a discharge specific capacity of  $894 \text{ mAh g}^{-1}$  (Figure S15), much lower than that using LiCl in the electrolyte. SEM image of the Mg anode after discharging is shown in Figure 4f. Instead of a loose and needle-like morphology, a uniform and dense passive layer was observed, and the EDS elemental mapping revealed that the passive layer mainly

consisted of O and Mg elements. The discharge product was also analyzed by XPS. The Mg 2p located at 48.9 eV and O 1s located at 531.42 eV indicated the existence of  $\text{Mg}(\text{OH})_2$  (Figure 4g and Figure S16).<sup>[39]</sup> Another Mg 2p peak located at 50.23 eV along with O 1s at 529.7 eV was attributed to the MgO produced by the oxidation of residual Mg.<sup>[39]</sup> The above results showed that the formation of the unique loosely needle-like discharge product should be related to the chlorine ion. On the other hand, the capacity of the Mg-air battery with a dense and uniform passive layer was much lower than the one with a loose and needle-like discharge product. Therefore, the unique needle-like discharge product was helpful to improve the discharge capacity of the Mg-air battery.

In conclusion, Mg-air batteries with ultrahigh average specific capacity of  $2190 \text{ mAh g}^{-1}$  and high energy density of  $2282 \text{ Wh kg}^{-1}$  had been achieved by designing a dual-layer gel electrolyte strategy. The organic gel protected the Mg anode

from corrosion and the chlorine ions in the hydrogel helped to produce unique needle-like discharge products, rather than a commonly reported dense passive layer. As a result, the electrolyte well contacted Mg anode and the discharge process continued until the Mg was almost entirely consumed. Besides, attributed to the unique coaxial structure of fiber shape and stable interface of the dual-layer gel electrolyte, the resulting fiber Mg-air battery not only performed high electrochemical properties but also exhibited high flexibility and stable output even after being immersed in water, which paves the way for powering wearable and implantable electronic devices in the future.

## Acknowledgements

This work was supported by the National Natural Science Foundation of China (22005137), Natural Science Foundation of Jiangsu Province (BK20200321), Fundamental Research Funds for the Central Universities (14380175, 14380187), National Postdoctoral Program for Innovative Talents (BX20200161) and Start-up Fund at Nanjing University (14912221).

## Conflict of interest

The authors declare no conflict of interest.

**Keywords:** flexible · gel electrolyte · high specific capacity · Mg-air battery

- [1] Y. Liu, J. Li, S. Song, J. Kang, Y. Tsao, S. Chen, V. Mottini, K. McConnell, W. Xu, Y. Zheng, J. B. Tok, P. M. George, Z. Bao, *Nat. Biotechnol.* **2020**, *38*, 1031–1036.
- [2] A. Moin, A. Zhou, A. Rahimi, A. Menon, S. Benatti, G. Alexandrov, S. Tamakloe, J. N. Ting, N. Yamamoto, Y. Khan, F. Burghardt, L. Benini, A. C. Arias, J. M. Rabaey, *Nat. Electron.* **2021**, *4*, 54–63.
- [3] X. Fu, L. Wang, L. Zhao, Z. Yuan, Y. Zhang, D. Wang, D. Wang, J. Li, D. Li, V. Shulga, G. Shen, W. Han, *Adv. Funct. Mater.* **2021**, *31*, 2010533.
- [4] L. Ma, S. Chen, X. Li, A. Chen, B. Dong, C. Zhi, *Angew. Chem. Int. Ed.* **2020**, *59*, 23836–23844; *Angew. Chem.* **2020**, *132*, 24044–24052.
- [5] C. Wang, T. He, J. Cheng, Q. Guan, B. Wang, *Adv. Funct. Mater.* **2020**, *30*, 2004430.
- [6] Y. Zhu, M. Yang, Q. Huang, D. Wang, R. Yu, J. Wang, Z. Zheng, D. Wang, *Adv. Mater.* **2020**, *32*, 1906205.
- [7] A. J. Bhandarkar, S. P. Lee, I. Huang, W. Li, S. Wang, C. Su, W. J. Jeang, T. Hang, S. Mehta, N. Nyberg, P. Gutruf, J. Choi, J. Koo, J. T. Reeder, R. Tseng, R. Ghaffari, J. A. Rogers, *Nat. Electron.* **2020**, *3*, 554–562.
- [8] Z. Pei, Z. Yuan, C. Wang, S. Zhao, J. Fei, L. Wei, J. Chen, C. Wang, R. Qi, Z. Liu, Y. Chen, *Angew. Chem. Int. Ed.* **2020**, *59*, 4793–4799; *Angew. Chem.* **2020**, *132*, 4823–4829.
- [9] W. Sun, F. Wang, B. Zhang, M. Zhang, V. Kupers, X. Ji, C. Theile, P. Bieker, K. Xu, C. Wang, M. Winter, *Science* **2021**, *371*, 46–51.
- [10] X. Jia, C. Wang, C. Zhao, Y. Ge, G. G. Wallace, *Adv. Funct. Mater.* **2016**, *26*, 1454–1462.
- [11] C. Cheng, S. Li, Y. Xia, L. Ma, C. Nie, C. Roth, A. Thomas, R. Haag, *Adv. Mater.* **2018**, *30*, 1802669.
- [12] C. Yu, C. Wang, X. Liu, X. Jia, S. Naficy, K. Shu, M. Forsyth, G. G. Wallace, *Adv. Mater.* **2016**, *28*, 9349–9355.
- [13] T. Zhang, Z. Tao, J. Chen, *Mater. Horiz.* **2014**, *1*, 196–206.
- [14] C. Li, Y. Sun, F. Gebert, S. Chou, *Adv. Energy Mater.* **2017**, *7*, 1700869.
- [15] Y. Li, X. Zhang, H. Li, H. D. Yoo, X. Chi, Q. An, J. Liu, M. Yu, W. Wang, Y. Yao, *Nano Energy* **2016**, *27*, 8–16.
- [16] M. Yuasa, X. Huang, K. Suzuki, M. Mabuchi, Y. Chino, *J. Power Sources* **2015**, *297*, 449–456.
- [17] X. Chen, Q. Liao, Q. Le, Q. Zou, H. Wang, A. Atrens, *Electrochim. Acta* **2020**, *348*, 136315.
- [18] Y. Wu, Z. Wang, Y. Liu, G. Li, S. Xie, H. Yu, H. Xiong, *J. Mater. Eng. Perform.* **2019**, *28*, 2006–2016.
- [19] M. M. Dinesh, K. Saminathan, M. Selvam, S. R. Srither, V. Rajendran, K. V. I. S. Kaler, *J. Power Sources* **2015**, *276*, 32–38.
- [20] S. Y. Liew, J. Juan, C. Lai, G. Pan, T. C. K. Yang, T. K. Lee, *Ionics* **2019**, *25*, 1291–1301.
- [21] X. Chen, Q. Zou, Q. Le, J. Hou, R. Guo, H. Wang, C. Hu, L. Bao, T. Wang, D. Zhao, F. Yu, A. Atrens, *J. Power Sources* **2020**, *451*, 227807.
- [22] Y. Feng, W. Xiong, J. Zhang, R. Wang, N. Wang, *J. Mater. Chem. A* **2016**, *4*, 8658–8668.
- [23] J. Wu, R. Wang, Y. Feng, C. Peng, *J. Alloys Compd.* **2018**, *765*, 736–746.
- [24] L. Ye, M. Liao, H. Sun, Y. Yang, C. Tang, Y. Zhao, L. Wang, Y. Xu, L. Zhang, B. Wang, F. Xu, X. Sun, Y. Zhang, H. Dai, P. G. Bruce, H. Peng, *Angew. Chem. Int. Ed.* **2019**, *58*, 2437–2442; *Angew. Chem.* **2019**, *131*, 2459–2464.
- [25] M. M. Abutalib, A. Rajeh, *Phys. B* **2020**, *578*, 411796.
- [26] M. A. Morsi, S. A. El-Khodary, A. Rajeh, *Phys. B* **2018**, *539*, 88–96.
- [27] X. Zhao, L. Wang, X. Chen, W. Wang, H. Xin, X. Du, J. Yang, *J. Power Sources* **2020**, *449*, 227482.
- [28] Y. Zhang, Y. Wang, L. Wang, C. Lo, Y. Zhao, Y. Jiao, G. Zheng, H. Peng, *J. Mater. Chem. A* **2016**, *4*, 9002–9008.
- [29] S. Li, Y. Liu, X. Zhao, Q. Shen, W. Zhao, Q. Tan, N. Zhang, P. Li, L. Jiao, X. Qu, *Adv. Mater.* **2021**, *33*, 2007480.
- [30] S. He, J. Wang, X. Zhang, J. Chen, Z. Wang, T. Yang, Z. Liu, Y. Liang, B. Wang, S. Liu, L. Zhang, J. Huang, J. Huang, L. A. O'Dell, H. Yu, *Adv. Funct. Mater.* **2019**, *29*, 1905228.
- [31] H. Sun, G. Zhu, Y. Zhu, M. Lin, H. Chen, Y. Li, W. H. Hung, B. Zhou, X. Wang, Y. Bai, M. Gu, C. Huang, H. Tai, X. Xu, M. Angell, J. J. Shyue, H. Dai, *Adv. Mater.* **2020**, *32*, 2001741.
- [32] T. Liu, J. Mou, Z. Wu, C. Lv, J. Huang, M. Liu, *Adv. Funct. Mater.* **2020**, *30*, 2003407.
- [33] Y. Xu, Y. Zhao, J. Ren, Y. Zhang, H. Peng, *Angew. Chem. Int. Ed.* **2016**, *55*, 7979–7982; *Angew. Chem.* **2016**, *128*, 8111–8114.
- [34] S. Ardizzone, C. L. Bianchi, M. Fadoni, B. Vercelli, *Appl. Surf. Sci.* **1997**, *119*, 253–259.
- [35] I. I. Pollini, *Phys. Rev. B* **1994**, *50*, 2095–2103.
- [36] J. T. Klopprogge, L. V. Duong, B. J. Wood, R. L. Frost, *J. Colloid Interface Sci.* **2006**, *296*, 572–576.
- [37] M. Yoshizawa, K. Ito-Akita, H. Ohno, *Electrochim. Acta* **2000**, *45*, 1617–1621.
- [38] J. Wu, Y. Xiao, J. Su, T. Deng, J. Feng, Y. Mo, M. Zeng, *Sci. China Technol. Sci.* **2011**, *54*, 682–690.
- [39] L. X. Li, D. Xu, X. Li, W. Liu, Y. Jia, *New J. Chem.* **2014**, *38*, 5445–5452.

Manuscript received: April 1, 2021

Revised manuscript received: April 9, 2021

Accepted manuscript online: April 29, 2021

Version of record online: June 9, 2021